



Contents lists available at ScienceDirect

Journal of Alloys and Compounds

journal homepage: www.elsevier.com/locate/jalcom

Influence of Ta on the oxidation resistance of WB_{2-z} coatings

C. Fuger^{a,*}, B. Schwartz^a, T. Wojcik^{a,b}, V. Moraes^b, M. Weiss^c, A. Limbeck^c, C.A. Macauley^{d,e}, O. Hunold^f, P. Polcik^g, D. Primetzhofer^h, P. Felber^d, P.H. Mayrhofer^b, H. Riedl^{a,b}

^a Christian Doppler Laboratory for Surface Engineering of high-performance Components, TU Wien, Austria

^b Institute of Materials Science and Technology, TU Wien, A-1060 Wien, Austria

^c Institute of Chemical Technologies and Analytics, TU Wien, Vienna, Austria

^d Department of Materials Science, Friedrich-Alexander-Universität Erlangen-Nürnberg, Germany

^e Interdisciplinary Center for Nanostructured Films (IZNF), 91058 Erlangen, Germany

^f Oerlikon Balzers, Oerlikon Surface Solutions AG, 9496 Balzers, Liechtenstein

^g Plansee Composite Materials GmbH, D-86983 Lechbruck am See, Germany

^h Department of Physics and Astronomy, Uppsala University, SE-75120 Uppsala, Sweden

ARTICLE INFO

Article history:

Received 18 September 2020

Received in revised form 22 November 2020

Accepted 24 November 2020

Available online xxx

Keywords:

Oxidation resistance
Transition metal diborides
Scale growth
Diborides

ABSTRACT

Ternary $W_{1-x}Ta_xB_{2-z}$ is a promising protective coating material possessing enhanced ductile character and phase stability compared to closely related binaries. Here, the oxidation resistance of $W_{1-x}Ta_xB_{2-z}$ thin films was experimentally investigated at temperatures up to 700 °C. Ta alloying in sputter deposited WB_{2-z} coatings led to decelerated oxide scale growth and a changed growth mode from parabolic to a more linear (but retarded) behavior with increasing Ta content. The corresponding rate constants decrease from $k_p^* = 6.3 \cdot 10^{-4} \mu\text{m}^2/\text{s}$ for WB_{2-z} , to $k_p^* = 1.1 \cdot 10^{-4} \mu\text{m}^2/\text{s}$ for $W_{0.66}Ta_{0.34}B_{2-z}$ as well as $k_l = 2.6 \cdot 10^{-5} \mu\text{m}/\text{s}$ for TaB_{2-z} , underlined by decreasing scale thicknesses ranging from 1170 nm (WB_{2-z}), over 610 nm ($W_{0.66}Ta_{0.34}B_{2-z}$) to 320 nm (TaB_{2-z}) after 10 min at 700 °C. Dense and adherent scales exhibit an increased tantalum content (columnar oxides), which suppresses the volatile character of tungsten-rich as well as boron oxides, hence being a key-factor for enhanced oxidation resistance. Thus, adding Ta (in the range of $x = 0.2-0.3$) to α -structured WB_{2-z} does not only positively influence the ductile character and thermal stability but also drastically increases the oxidation resistance.

© 2020 The Author(s). Published by Elsevier B.V.
CC BY 4.0

1. Introduction

Various industrial applications, e.g. in aerospace industry, aviation, or energy production, demand complex applied materials requirements to increase lifetime and thus, enhance environmental sustainability. Since bulk materials occasionally cannot fulfill all these demands, surface engineering using physical vapor deposition (PVD) deposited thin films is a well-established method enhancing specific properties. Based on the most common applications, transition metal ceramics, particularly transition metal nitrides such as TiN, CrN, or $Ti_{1-x}Al_xN$ have been explored in depth over decades [1–3]. However, the material class of borides is a valuable alternative in new applications. Especially, transition metal borides (TMBs) exhibit a tremendous potential to be applied in various fields ranging from wear and corrosion resistant coatings, to superconductive thin films, or as superhard and extremely stable protective layers in

diverse engineering applications [4–6]. One very interesting representative of the TMBs is tungsten diboride, which exhibits specific mechanical properties with respect to the generally limited fracture tolerance of such ceramic compounds [7–9]. Previous studies on diborides revealed that transition metal diborides tend to crystallize in two different hexagonal structures, α - (AlB_2 , space group 191, P6/mmm) and ω -prototype (W_2B_{5-x} , space group 194, P6₃/mmc), respectively [10,11]. By synthesizing WB_{2-z} coatings using PVD techniques, the films crystallize in the metastable α -phase rather than in the thermodynamically preferred ω -structure. As structural defects play a crucial role in the stabilization of α -structured WB_{2-z} , the impact on the mechanical properties, especially fracture resistance, is still not fully described. However, in theoretical as well as experimental investigations (by free-standing cantilever tests), α - WB_{2-z} exhibits a highly ductile behavior with K_{IC} values of around $3.7 \pm 0.3 \text{ MPa}\sqrt{\text{m}}$. In comparison, ZrB_{2-z} and $Zr_{1-x}Ta_xB_{2-z}$ films obtain values around from 3.5 to 5.5 $\text{MPa}\sqrt{\text{m}}$ during cube corner indentation, which typically overestimates fracture characteristics (compared to cantilever bending) by at least 2.0 $\text{MPa}\sqrt{\text{m}}$ [12–14]. However, one weak point of α -structured WB_{2-z} is the thermal

* Corresponding author.

E-mail address: christoph.fuger@tuwien.ac.at (C. Fuger).

<https://doi.org/10.1016/j.jallcom.2020.158121>

0925-8388/© 2020 The Author(s). Published by Elsevier B.V.
CC BY 4.0

stability, as the decomposition to its stable ω -modification sets in relatively early – at around 800 °C. Furthermore, in addition to the limited phase stability in inert atmospheres, the formation of volatile tungsten oxides occurs at even lower temperatures and thus strongly limits the wide usage of α -structured WB_{2-z} [15–17]. With respect to phase transition between α and ω , the addition of Ta has been proven to shift the starting point for decomposition to increased temperatures. The resulting ternary $W_{1-x}Ta_xB_{2-z}$ with $x \sim 0.25$ leads to an enhancement of the decomposition temperature (in inert atmosphere) by 600 °C to a maximum of $T_{dec} = 1400$ °C [18]. Small additions of Ta also slightly enhance the fracture toughness to 3.8 ± 0.5 MPa \sqrt{m} at $x \sim 0.15$, while obtaining hardness values above 40 GPa [12,18]. All these points suggest $W_{1-x}Ta_xB_{2-z}$ as a promising protective coating system. However, a clear study of the influence of Ta on the oxidation resistance is still missing to complete the profile of properties.

Therefore, based on the above-mentioned results, the focus of this study is to investigate in detail the influence of Ta on the oxidation resistance of sputter deposited $W_{1-x}Ta_xB_{2-z}$ thin films.

2. Experimental

All WB_{2-z} , $W_{1-x}Ta_xB_{2-z}$, and TaB_{2-z} coatings were deposited by DC magnetron sputtering using an in-house developed deposition system with two confocal arranged cathodes, for details see [19]. The ultra-high vacuum coating facility was equipped with two 6-inch – TaB_2 and W_2B_5 – powder-metallurgically produced targets obtaining a purity of at least 99.6% (Plansee Composite Materials GmbH). Prior to the depositions, the silicon ($20 \times 7 \times 0.33$ mm³, 100-oriented) and single crystalline sapphire ($10 \times 10 \times 0.5$ mm³, 012-oriented) substrates were ultrasonically pre-cleaned in acetone and ethanol for 5 min each. Subsequently, they were mounted on a rotating substrate holder, and heated up in the chamber (base pressure below $4 \cdot 10^{-4}$ Pa) to the deposition temperature, T_{dep} , of 500 °C (corresponding to 300 ± 15 °C on the substrate surface) for at least 20 min. Furthermore, the substrates were etched in argon atmosphere ($p_{etch} = 6$ Pa) for 10 min applying a substrate potential of –500 V. The deposition process itself was carried out in pure argon atmosphere at a deposition pressure of 0.4 Pa. Both targets were powered by a Solvix HIP³ generator – used in DC mode – controlling the applied target current, I_{target} , of maximum 4.2 A in total for both cathodes. To vary the chemical composition of the deposited films (dividing the full compositional range in steps of about $x \sim 0.20$) the applied current was changed successively for both target materials. The deposition time was varied between 60 and 85 min due to a decreased sputter rate for TaB_2 with respect to W_2B_5 . To gain homogeneous compositions over all substrates, the substrate holder was rotated with a frequency, f_{rot} , of 0.25 Hz. The film growth was also supported by applying a bias potential of –50 V.

All oxidation tests were carried out in a standard chamber furnace in ambient air. To gain relatively flat and defined oxide scales, all oxidation tests have been performed on sapphire substrates. The kinetic behavior of the oxide scale formation was analyzed through varying the exposure time ($t_{ox} = 1, 10, 100,$ and 1000 min) and temperature ($T_{ox} = 500, 600,$ and 700 °C), respectively. The temperatures and time periods were selected based on oxidation pretests. In detail, all compositions have been fully oxidized after 1000 min at 700 °C and therefore the oxidation temperature was not further increased. After quantifying the oxide scale thicknesses by means of scanning electron microscopy (SEM) investigations (FEI Quanta 200 FEG-SEM) within fracture cross-sections, the oxidation rate constants were calculated by linear regression of squared oxide thickness values as a function of oxidation time.

As a proper chemical quantification of light elements in combination with heavy ones e.g. $W_{1-x}Ta_xB_{2-z}$, presents a certain challenge [18], different chemical analysis methods were utilized to obtain best

results. The elemental composition of all as deposited thin films on Si substrates was analyzed by liquid inductively coupled plasma optical emission spectroscopy (ICP-OES). Liquid ICP-OES measurements were carried out on an iCAP 6500 RAD (Thermo Fisher Scientific, USA), with an ASX-520 autosampler (CETAC Technologies, USA) using a HF resistant sample introduction kit, consisting of a Miramist nebulizer (Burger Research, USA), a PTFE spray chamber and a ceramic injector tube. All $W_{1-x}Ta_xB_{2-z}$ coatings were acid digested with the method presented and validated in [20]. Samples were broken into pieces of about 3×3 mm² and the thin film with the substrate was dissolved in a mixture of 1 mL HNO_3 and 0.25 mL HF. After a reaction time of 15 min at a temperature of 60 °C, the thin films including the substrates were completely dissolved. Derived sample digests were diluted to a final volume of 20 mL with a mixture of 3% HNO_3 and 0.3% HF. Quantification was done via external calibration using matrix adjusted standards - for further details see also [20–22].

For a 3D elemental distribution, a selected coating in the as deposited state was analyzed by atom probe tomography (APT). The APT analysis was carried out on a CAMECA LEAP 4000X HR in pulsed laser mode. This instrument is equipped with a 355 nm UV laser with a spot size of ~ 2 μ m and a reflectron lens resulting in a detection efficiency of $\sim 37\%$. The experiments were done with a laser pulse energy of 50 pJ at a target evaporation rate of 1%. The as-deposited samples were extracted using a keyhole technique [23], which places the analysis axis in the growth direction of the film. Moreover, the composition of selected as deposited samples as well as compositional depth profiles of the oxide layers were obtained by time of flight elastic recoil detection analysis (TOF-ERDA) using a 36 MeV I^{8+} ion beam and detecting recoils in a detection angle of 45° with respect to the primary beam. Details on the employed detection system can be found in Ström et al. [24]. The expected systematic uncertainties for light elements such as B are found on a level of ± 1 at% for relative measurements free from standards, mainly due to uncertainties in the specific energy loss of the recoiling particles. For absolute measurements (free from standards), systematic uncertainties for light elements (e.g. B or C) are expected to be on a level of 5–10% of the detected concentration. A detailed description of sources and consequences of systematic uncertainties are discussed in more detail by Arvizu et al. [25] and Zhang et al. [26]. Depth profiles were established using the CONTES software package [27].

The coating morphology – before and after oxidation – was analyzed in cross sectional view by a FEI Quanta 250 FEG-SEM, equipped with a field emission gun (acceleration voltage used, 10 kV). In addition, the chemical composition of the formed scales and unaffected coatings was analyzed by energy dispersive X-Ray spectroscopy (EDAX EDS detector, 15 kV acceleration voltage). Selected samples were also surveyed in cross sectional view by transmission electron microscopy (TEM FEI TECNAI, G20, acceleration voltage of 200 kV). Detailed structural information of the formed oxide scales was gained by selected area electron diffraction (SAED) analysis. The sample preparation was done by focused ion beam (FIB, Quanta 200 3D Dual Beam), applying standard lift out techniques [28].

3. Results and discussion

3.1. Chemical composition and phase constitution as deposited

After sputter depositing the films, the chemical compositions of all coatings have been analyzed by ICP-OES. Fig. 1 shows the boron content (in at%) of all deposited coatings as a function of the Ta fraction at the metal sublattice, x . The blue, half-filled triangles are indicating the chemical compositions of the films synthesized within this study, while the green open squares are highlighting the

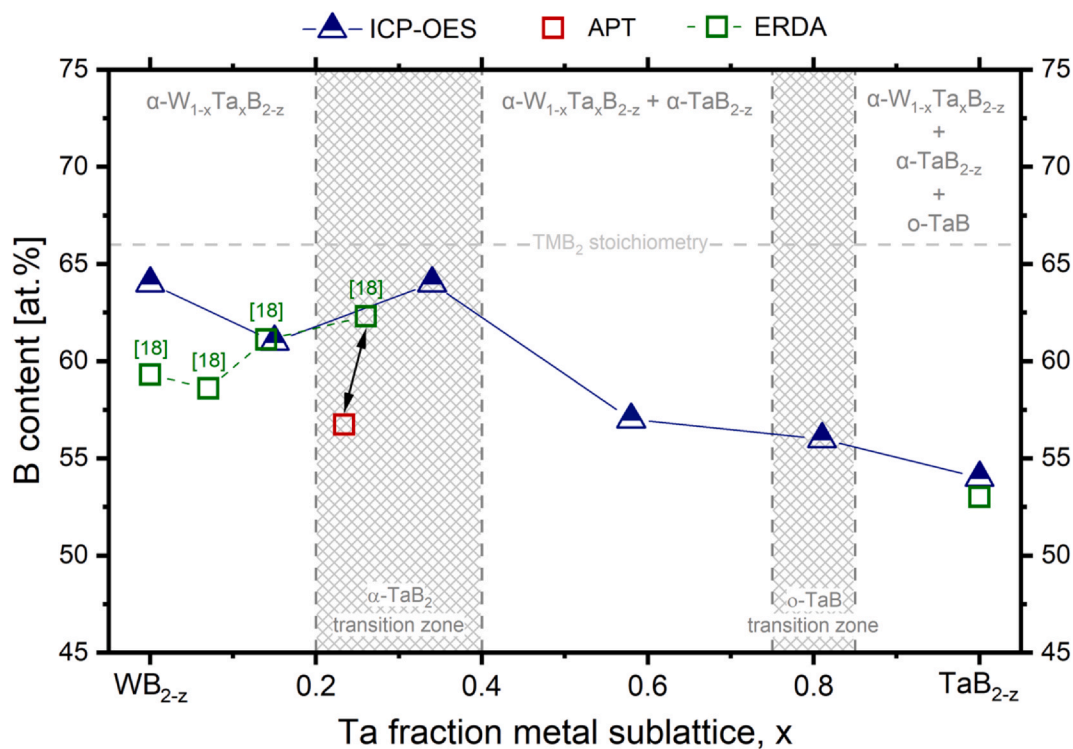


Fig. 1. Chemical composition obtained by ICP-OES of all coatings deposited within this study (blue data points). The green data points indicate the chemical composition evaluated by TOF-ERDA of $W_{1-x}Ta_xB_{2-z}$ thin films taken from [18] – except TaB_{2-z} which was analyzed within this study. During APT the overall elemental concentration of the inspected tip was evaluated and is indicated in red. (For interpretation of the references to colour in this figure legend, the reader is referred to the web version of this article.)

elemental fraction of $W_{1-x}Ta_xB_{2-z}$ coatings (obtained by TOF-ERDA) prepared in a previous study [18]. For a further comparison between different analysis techniques as well as quality and reproducibility of the depositions, the average W, Ta (in terms of metal sublattice occupation, x) and B concentration of a surveyed atom probe tip is also given in Fig. 1, see red open square (selected coating originates from study [18] – analyzed volume is depicted in Fig. 2). Both studies (blue and green data set refer to this study and Ref. [18]) exhibit the similar tendency of decreasing boron content with increasing amount of tantalum, highlighting the strong affinity to form either sub-stoichiometric structures with boron and/or Schottky defects as well as multi-phased coatings. Nevertheless, the decreasing B contents with increasing Ta are a strong indication, that the phase formation of α -structured $W_{1-x}Ta_xB_{2-z}$ films at high Ta fractions is limited and directed towards dual phase structures (α - $W_{1-x}Ta_xB_{2-z}$ + α - TaB_{2-z} or an orthorhombic o - TaB phase) – as also suggested in [12]. By considering all chemical and structural data (X-Ray diffraction [XRD] pattern for the full compositional range are presented in the Appendix), we can assume that there is a more or less ideal solid solution of α - $W_{1-x}Ta_xB_{2-z}$ up to about $x = 0.20$ (on the metal sublattice) and dual phased morphologies containing α - $W_{1-x}Ta_xB_{2-z}$ as well as α - TaB_{2-z} rich domains at Ta concentrations $x > 0.40$. Furthermore, at $Ta > 0.85$ an additional o - TaB phase is occurring. The gray shaded areas between $x = 0.20$ – 0.40 as well as 0.75 – 0.85 exhibit the transition zones of upcoming TaB_2 / TaB rich domains and the change between α -dominated structures and the additional appearance of a o - TaB phase, respectively.

To reveal a more detailed picture about the 3D atomic composition in the so-called α - TaB_2 transition zone ($x \geq 0.26$, Ta sublattice occupation), a detailed ATP analysis of the $W_{0.74}Ta_{0.26}B_{1.89}$ (given composition obtained by TOF-ERDA) coating was conducted (see Fig. 2a). The inhomogeneous distribution of tantalum in the growth direction, is shown clearly in the one-dimensional concentration profile (see Fig. 2b). Both, Ta and W show an inversely oscillating concentration going from ~ 5 at% to ~ 15 at% for Ta ($x = 0.12$ – 0.37 Ta

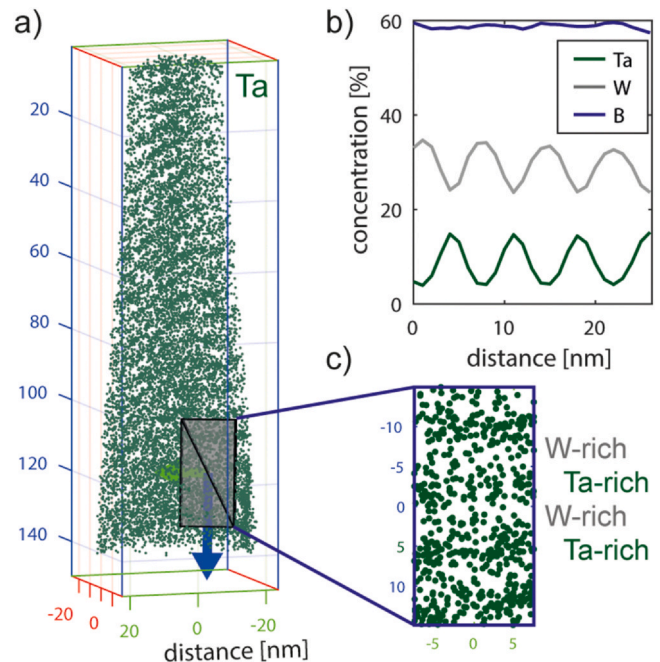


Fig. 2. Elemental distribution of Ta obtained by atom probe tomography of $W_{0.74}Ta_{0.26}B_{2-z}$ coating (a), showing a horizontally layered structure also confirmed by the one-dimensional concentration profile, depicted in (b). The layered structure is characterized by an alternating W/Ta content, highlighted by the image detail (c).

occupation on the metal sublattice) and from ~ 35 at% to ~ 25 at% for W ($x = 0.88$ – 0.63 W sublattice occupation). This behavior could be due to, (i) a limited solubility of Ta in the α - $W_{1-x}Ta_xB_{2-z}$ structure, indicating the occurrence of a Ta rich phase and/or (ii) a synthesis related effect through the experimental setup of co-sputtering a WB_{2-z} and TaB_{2-z} targets, respectively. By taking into account the

rotational frequency of the substrate holder (0.25 Hz) and the deposition rate of both binary systems (~ 70 nm/min for WB_{2-z} compared to ~ 50 nm/min for TaB_{2-z}) result in an overall deposition rate of ~ 5 nm/s, which fits to the periodicity in Fig. 2b. Assuming that the substrate holder is not fully covered from both, the WB_{2-z} and TaB_{2-z} sputter plumes, there are areas with increased WB_{2-z}/TaB_{2-z} concentration, dependent on the progress of rotation. Therefore, the layered structure, depicted in Fig. 2, is suggested to be an unintended variation caused by the co-sputtering process [29]. Nevertheless, a limited solubility of Ta in the $\alpha-W_{1-x}Ta_xB_{2-z}$ structure cannot be ruled out, as the W-depleted sections reveal $x \sim 0.37$ Ta on the metal sublattice (overall ~ 15 at% Ta). A more detailed view of the alternating W/Ta rich sections is also given in the cutout, depicted in Fig. 2c. Due to reasons of clarity, W atoms are not visualized in Fig. 2. These detailed analyses are also in good agreement with the diffraction results, which suggests that samples in the $\alpha-TaB_2$ transition zone ($x \geq 0.26$) form imperfect as-deposited solid solutions when deposited using co-sputtering. Nevertheless, the occurrence of multi-phased coatings containing $\alpha-W_{1-x}Ta_xB_{2-z}$, $\alpha-TaB_{2-z}$, as well as o-TaB is mostly related to a lack of boron and the high tendency to form stoichiometric o-TaB. (please place Figure 2 here)

Nevertheless, a well-known deviation regarding the boron content of APT, TOF-ERDA and ICP-OES evaluated samples is also visible within this study – especially, depicted by the green (TOF-ERDA) and red square (APT), indicating a thin film from the same deposition run. To obtain comparable values, impurities like H, C, O, N and Ga have been subtracted from the total concentration of the APT tip, as all these elements together have been less than 2 at%. Here, we need to mention that the analyzed volume during APT is way smaller compared to the other analysis techniques. Nonetheless, the data sets from all utilized analysis techniques clearly reveal that the detection of an absolute boron concentration is difficult and only comparable when originating from the same technique/set-up as highlighted by [30,31]. However, the amount of W and Ta atoms shows almost perfect coincidence between APT and TOF-ERDA. To simplify notations, we therefore used TMB_{2-z} within the manuscript (always normalized to the metal sublattice).

3.2. Oxide scale formation

As a constant film thickness is crucial for a clear comparison during oxidation tests, the deposition times were adapted (from 60 to 85 min with increasing Ta) to grow films between 3.5 and 4.0 μm for all compositions. Cross sectional micrographs obtained with SEM, revealed very dense and smooth morphologies for all coatings in the as deposited state (on Si substrate) – see Fig. 3a-i for WB_{2-z} , 3b-i for $W_{0.42}Ta_{0.58}B_{2-z}$, and 3c-i for TaB_{2-z} , respectively. In contrast to our previous study, showing a more pronounced columnar growth morphology, the coatings exhibited a rather fine-grained to amorphous, nearly featureless structure. This is mainly attributed to the decreased deposition temperature used, $T_{\text{dep}} = 500$ $^{\circ}\text{C}$ compared to $T_{\text{dep}} = 700$ $^{\circ}\text{C}$ in [12].

In addition to the as deposited state, the corresponding cross-sectional micrographs after 100 min at 600 $^{\circ}\text{C}$ (3a-ii, 3b-ii, and 3c-ii) as well as 100 min at 700 $^{\circ}\text{C}$ (3a-iii, 3b-iii, and 3c-iii) oxidation are also presented. The coatings show stable oxide growth after 100 min at 600 $^{\circ}\text{C}$ and a decreased scale thickness with increasing Ta content (see Fig. 3-ii). However, after 100 min at $T_{\text{ox}} = 700$ $^{\circ}\text{C}$ all coatings reveal extensive oxide scales suggesting imminent break-through oxidation, which is also underlined by the presence of lateral cracks (see Fig. 3c-iii). Beyond $t_{\text{ox}} = 100$ min at $T_{\text{ox}} = 700$ $^{\circ}\text{C}$ all coatings start to spall off, and therefore no 1000-min oxidation tests at that temperature have been conducted. However, all scale thicknesses as well as scale morphologies were visually and analytically inspected by cross sectional SEM investigations.

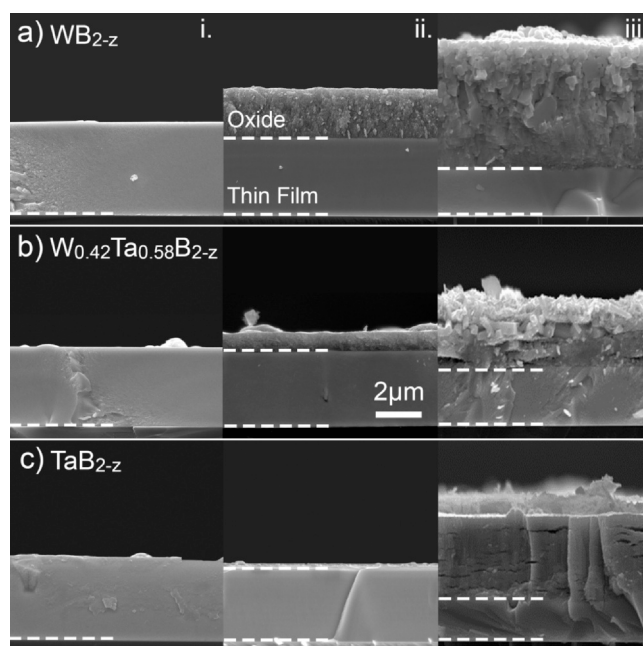


Fig. 3. Cross sectional micrographs of (a) WB_{2-z} , (b) $W_{0.42}Ta_{0.58}B_{2-z}$ and (c) TaB_{2-z} . Sections (a) – (c) show selected coatings in (i) as deposited state, (ii) after 100 min of oxidation at 600 $^{\circ}\text{C}$ and (iii) after 100 min of oxidation at 700 $^{\circ}\text{C}$. The dashed lines are highlighting the interface between substrate and thin film as well as between thin film and oxide scale (from bottom to top).

The oxide scale thicknesses in relation to the oxidation times are summarized exemplarily for all compositions oxidized at $T_{\text{ox}} = 600$ $^{\circ}\text{C}$ – see Fig. 4a. In general, the results clearly reveal decreasing oxide thickness with increasing Ta content – i.e. by comparing WB_{2-z} to TaB_{2-z} . The scale thickness significantly decreases from 8.0 μm for WB_{2-z} compared to 1.6 μm for TaB_{2-z} after $t_{\text{ox}} = 1000$ min. Furthermore, the growth mode changes from a more parabolic behavior for W-rich coatings to a more linear mode with increasing Ta content. This is in good agreement with the pure metals, as described by Kubaschewski and Hopkins [32]. Nevertheless, the more linear growth mode for the Ta-rich coatings seems to be retarded – which could be related to the morphology and density of the formed oxide – compared to the parabolic behavior for WB_{2-z} rich coatings. Unfortunately, there is no datapoint for the $W_{0.19}Ta_{0.81}B_{2-z}$ coating (purple diamond) after 1000 min at $T_{\text{ox}} = 600$ $^{\circ}\text{C}$ of oxidation because of spallation (see purple diamonds in Fig. 4a).

3.3. Oxidation kinetics

To gain further information about the oxidation kinetics, the rate constants k_p^* (for parabolic scale growth dominated by bulk and grain boundary diffusion – also called “Regime 2”) and k_l (for linear rate law dominated by surface reaction of oxygen – so called “Regime 1”) were calculated according to the procedure described in [33]. The calculations yield to an oxidation rate constant of $k_p^* = 6.3 \cdot 10^{-4}$ $\mu\text{m}^2/\text{s}$ (oxidation is following a parabolic growth mode) for WB_{2-z} (full squares) which is decreasing to $k_l = 2.6 \cdot 10^{-5}$ $\mu\text{m}/\text{s}$ (linear oxidation growth mode, but one order of magnitude lower) for TaB_{2-z} (full stars). Coatings with a Ta content of $x = 0.34$ – 0.58 show a similar oxidation behavior, resulting in k_p^* values of around $1.1 \cdot 10^{-4}$ $\mu\text{m}^2/\text{s}$. Based on this dataset, the oxidation kinetics of $W_{0.19}Ta_{0.81}B_{2-z}$ is suggested to be similar. The subsections (b–d) of Fig. 4 depict the oxidation behavior of pure WB_{2-z} , $W_{0.42}Ta_{0.58}B_{2-z}$ and pure TaB_{2-z} , respectively, at T_{ox} of 500, 600, and 700 $^{\circ}\text{C}$. The oxide scales increase drastically for $T_{\text{ox}} = 700$ $^{\circ}\text{C}$ already after $t_{\text{ox}} = 100$ min, leading to lateral cracks (see Fig. 3c-iii) and moreover, to non-adherent scales. The abovementioned gradients in chemical composition due to

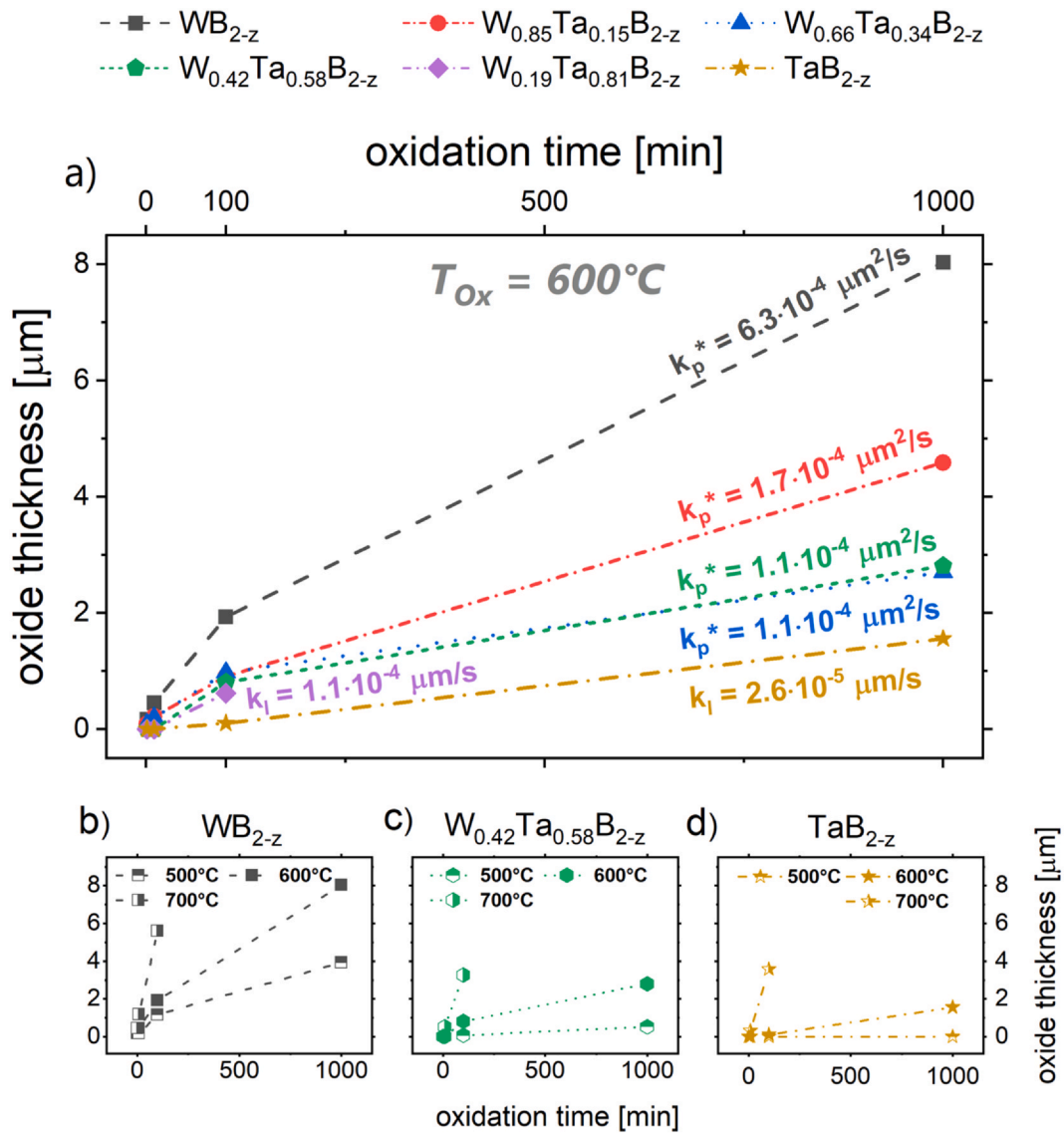


Fig. 4. Oxide thickness as a function of oxidation time for (a) 600 $^\circ\text{C}$, of all coatings deposited. The oxidation rate constants k_p (parabolic or paralineal growth mode) and k_l (linear growth mode) are depicted in section (a) indicated by individual symbols representing different coating compositions (see legend). Furthermore, the oxidation behavior of (b) WB_{2-z} , (c) $\text{W}_{0.42}\text{Ta}_{0.58}\text{B}_{2-z}$ and (d) TaB_{2-z} for 500, 600, and 700 $^\circ\text{C}$ oxidation temperature is represented. (For interpretation of the references to colour in this figure legend, the reader is referred to the web version of this article.)

co-sputtering may lead to this behavior, but also stress relief due to oxide scale formation in general can be a possible scenario. However, increased Ta contents clearly retard the oxide scale formation.

3.4. Oxide scale morphology

For a more detailed view on the oxide scale morphology and structure, TEM investigations of WB_{2-z} , $\text{W}_{0.66}\text{Ta}_{0.34}\text{B}_{2-z}$, and TaB_{2-z} after oxidizing at 700 $^\circ\text{C}$ for 10 min have been conducted. The results for $\alpha\text{-WB}_{2-z}$, $\alpha\text{-W}_{0.66}\text{Ta}_{0.34}\text{B}_{2-z}$, as well as multi-phased $\alpha\text{-TaB}_{2-z} + \text{o-TaB}$ are presented in Figs. 5–7, respectively. Fig. 5a depicts a cross sectional bright-field (BF) image of the unaffected coating and scale on top (from left to right hand side). Here, the highly fine-grained growth morphology of the unaffected WB_{2-z} coating is conceivable as no features are visible. In contrast, the thermally grown scale exhibits a granular-like, dense structure that is coarser towards the outermost regions. The Pt layer on top was deposited during FIB preparation of the TEM lamella. High resolution images – see Fig. 5b and c – show a fine-grained and dense oxide morphology near the coating-oxide interface (see Fig. 5b), whereas at the outermost

region relatively large (about ~ 100 nm) crystallites are formed (see Fig. 5c). This morphological change of the oxide with increasing thickness is possibly related to the changing growth mode of the forming WO_3 crystals, whereby the outermost regions undergo the longest oxidation time and consequently ongoing diffusion (having also the strongest oxygen supply). However, this area is also slightly porous at some positions. SAED also emphasizes the formation of a WO_3 crystals, see indexed pattern in Fig. 5d.

Fig. 6a shows a Scanning TEM – high angle annular dark-field (STEM-HAADF) image of the oxidized $\text{W}_{0.66}\text{Ta}_{0.34}\text{B}_{2-z}$ thin film. The formed oxide scale exhibits fine crystallites embedded in an amorphous matrix, also showing lateral cracks near the coating-oxide interface (see BF image in Fig. 6b). Here, the crack formation is related to the growth of WO_{3-x} and $\text{Ta}_2\text{O}_{5-x}$, which possess different thermal expansion coefficients ($\text{WO}_3 \sim 12 \cdot 10^{-6} \text{C}^{-1}$, $\text{Ta}_2\text{O}_5 \sim 4 \cdot 10^{-6} \text{C}^{-1}$ [34,35]) also with respect to the unaffected $\text{W}_{0.66}\text{Ta}_{0.34}\text{B}_{2-z}$ coating material. The difference in CTE needs also to be seen with respect to the unintended variation of the chemical composition originating from the co-sputtering process – see APT investigations in Fig. 2 – and hence suggesting for a partly layered oxide scale and related crack formation. Compared

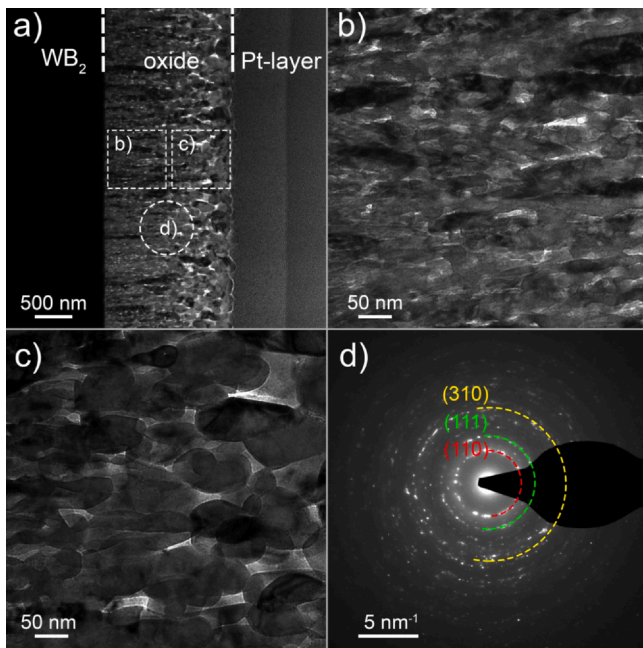


Fig. 5. Detailed TEM investigations of an oxidized WB_{2-z} coating after oxidation at $700\text{ }^{\circ}\text{C}$ for a duration of 10 min. Section (a) shows a bright-field (BF) TEM cross section of the oxidized coating, pointing out the areas for the HR images displayed in (b) and (c) and the recorded SAED shown in (d). The indicated ring patterns correspond to a WO_3 crystal.

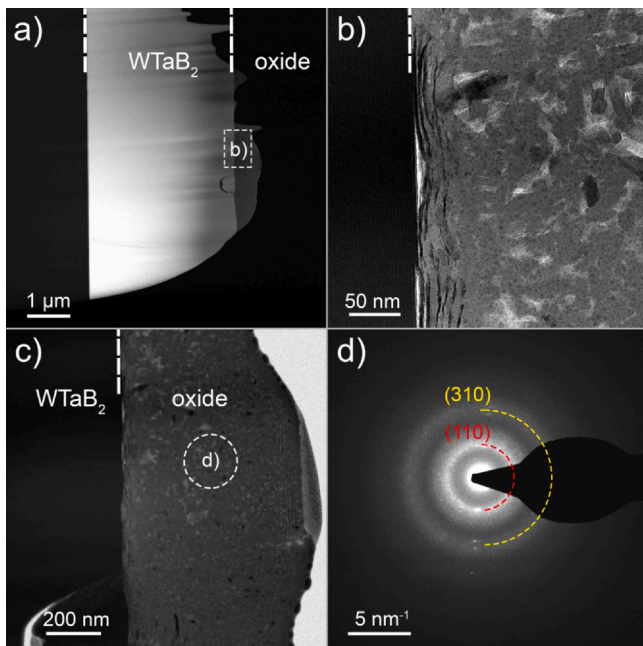


Fig. 6. Detailed TEM investigations of an oxidized $W_{0.66}Ta_{0.34}B_{2-z}$ coating after oxidation at $700\text{ }^{\circ}\text{C}$ for a duration of 10 min. Section (a) shows a STEM-HAADF cross section of the oxidized coating, pointing out the area for the BF image displayed in (b). Another BF cross section is depicted in (c) indicating the recorded SAED shown in (d).

to the oxide grown on pure WB_{2-z} , the crystallite size of the oxide that originates from $W_{0.66}Ta_{0.34}B_{2-z}$ stays rather constant over the entire scale (BF micro-graph, Fig. 6c). The amorphous oxide scale is also highlighted by the SAED pattern, depicted in Fig. 6d. However, WO_3 based crystallites can be indicated considering the very broad ring-shaped patterns as depicted in Fig. 6d. (Please place Figure 6 here)

Fig. 7a displays a BF cross section of the oxidized TaB_{2-z} coating, pointing out the areas for recorded SAED (Fig. 7b) and higher

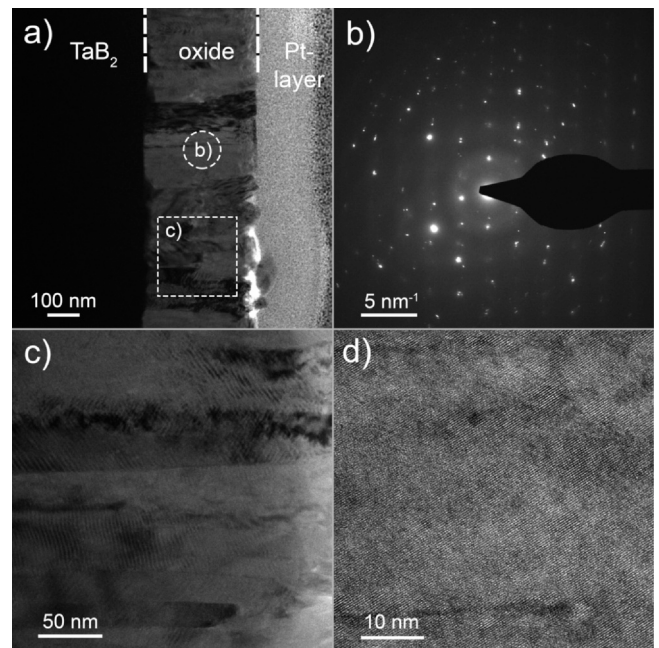


Fig. 7. TEM micrographs of an oxidized TaB_{2-z} coating after oxidation at $700\text{ }^{\circ}\text{C}$ for a duration of 10 min. Section (a) shows a BF TEM cross section of the oxidized coating, pointing out the areas for the recorded SAED displayed in (b) and the detailed BF image of the oxide scale shown in (c). An even more detailed view (high magnified-TEM) on the oxide is depicted in (d).

resolution BF image (Fig. 7c) of the formed oxide scale. Here, the very dense, columnar growth morphology with grain sizes up to 100 nm is very remarkable. Unfortunately, it was not possible to allocate the SAED pattern, which can be seen in Fig. 7b, to one distinct crystal structure. As the oxide layer on top of the TaB_2 film is composed of various grains revealing different crystal orientations and potentially different crystal structures, a very diffuse diffraction pattern appears. Nevertheless, Ta_2O_5 (in both versions orthorhombic [SG 25, Pmm2] as well as trigonal [SG 146, R3]) and $TaBO_4$ (orthorhombic [SG 141, I4₁/amd]) crystal structures revealed the best and most reliable matches in terms of the depicted SAED pattern. (Please place Figure 7 here)

3.5. Oxide scale constitution

To get a deeper insight into the oxide scale constitution, EDS investigations of oxidized WB_{2-z} , $W_{0.66}Ta_{0.34}B_{2-z}$, and TaB_{2-z} coatings were performed during TEM – again after oxidizing at $700\text{ }^{\circ}\text{C}$ for 10 min. In Fig. 8 the chemical composition is plotted as a function of the distance, which is highlighted in the STEM cross sections next to the EDS plots. A clear distinction between the oxide scale and the unaffected diboride coatings is possible for all three compositions. The EDS line scan in Fig. 8a reveals a W to O ratio of around 1–3, which indicates the occurrence of a WO_3 based scale – confirming the SAED results in Fig. 5d. However, also small amounts of boron can be detected, but being not dominant for the scale constitution and related to residuals during a volatile boron-oxide formation. Increasing the Ta content within the film also lead to a change in the scale constitution, as suggested by the line scan presented in Fig. 8b. The chemical composition depicted in Fig. 8b suggests for a highly oxygen rich scale, but still containing a certain amount of B. This is in good relation with the structural analysis of the scale presented in Fig. 6d indicating an amorphous state of the formed oxide scale, as boron oxide rich scales tend to be amorphous. Nevertheless, the metal (W,Ta) to O ratio is in the range of 1:4 emphasizing a change in the scale constitution. Additionally, the chemical composition of the

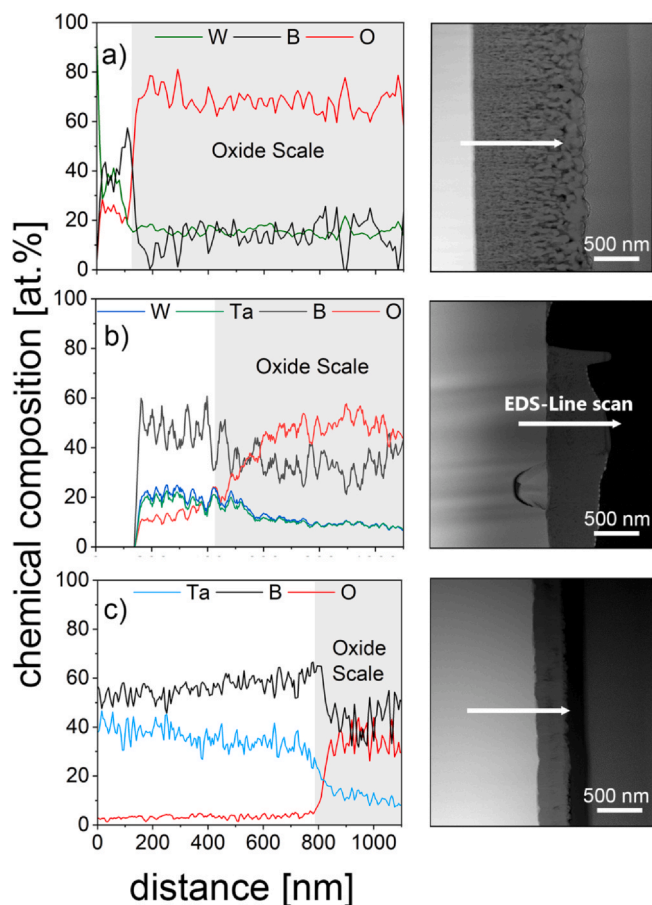


Fig. 8. EDS line scan of WB_{2-z} (a), $W_{0.66}Ta_{0.34}B_{2-z}$ (b) and TaB_{2-z} (c) thin films after oxidation with $700^\circ C$ for 10 min. The corresponding STEM micrographs on the right-hand side, indicate location and distance (white arrow – the tail refers to zero distance) of the performed EDS measurements. The uncertainty of quantifying light elements (like B and O) in EDS measurements can be in the range of 5–10%.

oxidized TaB_{2-z} coating (see Fig. 8c) underlines this trend, that the presence of Ta lead to a decelerated (volatile) boron oxide formation. The chemical analysis suggests for mixed oxide structures such as Ta_2O_5 and $TaBO_4$ – being in correspondence with the structural analysis in Fig. 7b.

As it is very difficult to gain reliable values for boron (and partly oxygen) contents with EDS, the chemical composition of the formed oxide scales, after 100 h at $600^\circ C$, was also investigated by TOF-ERDA. Due to resolution limits regarding the distinction of heavy W and Ta atoms, the elemental amount of tungsten and tantalum is summarized in a single dataset (blue lines). Fig. 9a reveals a boron depleted oxide layer (at least ~ 200 nm from the top of the oxide) on top of the WB_2 coating, indicating a clear volatile character of boron oxides during oxidation tests. However, the gradually increasing B contents for the Ta rich coatings as $W_{0.19}Ta_{0.81}B_{2-z}$ or pure TaB_{2-z} suggest a change from the volatile behavior to a more partly-viscous (glassy) character of the boron oxide through Ta. A similar tendency was also observed in the EDS line scans conducted during TEM analysis – see Fig. 8. TOF-ERDA provides information about the number of recoiled atoms per area, which were hit by impinging heavy ions, represented by the depth value plotted on the abscissa in Fig. 9. Therefore, the theoretical layer thickness can be calculated by means of the density and the molar weight of the containing elements. For the measured oxides on TaB_{2-z} coatings, the interface between oxide layer and coating was suggested to be located at around 500×10^{15} atoms/cm², where no more oxygen could be detected (see Fig. 9c). The atomic density of the oxide (assuming a

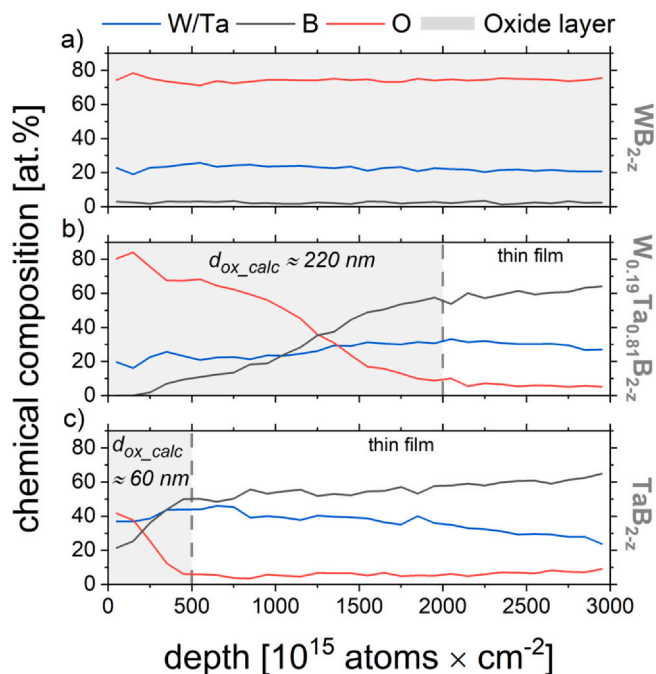


Fig. 9. Chemical composition of the oxide layers of WB_{2-z} (a), $W_{0.19}Ta_{0.81}B_{2-z}$ (b), and TaB_{2-z} (c) thin films after oxidation at $600^\circ C$ for 100 min, investigated by TOF-ERDA depth profiling. The gray area indicates the calculated oxide thickness by assuming a WO_3 structured oxide for WB_2 , and mixed oxide phases for $W_{0.19}Ta_{0.81}B_{2-z}$ as well as TaB_{2-z} .

mean value of 8.4 g cm^{-3} considering orthorhombic and trigonal Ta_2O_5 as well as orthorhombic $TaBO_4$) leads to a calculated layer thickness (d_{ox_calc}) of ~ 60 nm. Of course, the calculations do not consider boron oxide-based structures which are present to small quantities (as seen in the EDS linescans and ERDA profiles). As SEM investigations revealed an oxide thickness of ~ 100 nm after oxidation at $600^\circ C$ and 100 min, a slightly under-dense ($\sim 60\%$ density) oxide layer or a gradually variety/mixed oxide (leading to deviating densities) on TaB_{2-z} films is presumed. In Fig. 9b the calculated oxide thickness for $W_{0.19}Ta_{0.81}B_{2-z}$ was ~ 220 nm leading to a density of $\sim 40\%$ - relative to a measured oxide thickness of around 600 nm. Here we applied a weighted atomic density for the oxide, in correspondence to the line scan presented in Fig. 8b, of about 8.2 g cm^{-3} . Unfortunately, the penetration depth of ERDA was too low for detecting the oxide/coating interface of WB_{2-z} (see Fig. 9a). Hence, no thickness and oxide density could be calculated for pure WB_{2-z} . Nevertheless, an even lower oxide density compared to Ta-alloyed coatings is suggested by analyzing the TEM images represented in the foregoing Figures. These results lead to the assumption that the addition of Ta not only decreases the oxide scale growth kinetics but also increases the scale density.

4. Conclusion

To investigate the oxidation resistance of $W_{1-x}Ta_xB_{2-z}$ coatings, compositions in the full range from WB_{2-z} , $W_{0.85}Ta_{0.15}B_{2-z}$, $W_{0.66}Ta_{0.34}B_{2-z}$, $W_{0.42}Ta_{0.58}B_{2-z}$, $W_{0.19}Ta_{0.81}B_{2-z}$, to TaB_{2-z} were deposited by DC magnetron co-sputtering utilizing W_2B_5 and TaB_2 targets, respectively. ICP-OES as well as TOF-ERDA exhibit similar tendency of decreasing B contents with increasing amounts of tantalum, indicating that the phase formation of α -structured $W_{1-x}Ta_xB_{2-z}$ films at high Ta fractions is limited and directed towards dual phase structures (α - TaB_{2-z} and o- TaB). As highlighted by atom probe tomography, a layered structure composed of Ta-rich and W-rich zones is occurring at the nanoscale (in the range of 5–10 nm) – but it is assumed to be an artifact of co-sputtering.

After oxidation tests in ambient air at 500, 600, 700 °C for 1, 10, 100 and 1000 min, respectively, the formed oxide layers were analyzed by SEM, TEM, and TOF-ERDA. The investigations showed a decrease in oxide layer thickness with increasing Ta content for all temperature settings. At $T_{\text{ox}} = 600$ °C and $t_{\text{ox}} = 100$ min the oxide scale thickness decreases steadily from 2.2 μm to 0.1 μm from WB_{2-z} to TaB_{2-z} . A detailed evaluation of the oxidation kinetics revealed a parabolic scale growth for W-rich coatings becoming more linear but retarded with increasing Ta. The corresponding rate constants decelerate from $k_p^* = 6.3 \cdot 10^{-4} \mu\text{m}^2/\text{s}$ for

WB_{2-z} to $k_1 = 2.6 \cdot 10^{-5} \mu\text{m}/\text{s}$ (linear oxidation growth mode) for TaB_{2-z} . After 100 min at $T_{\text{ox}} = 700$ °C all coatings exhibit extensive scaling suggesting imminent break-through oxidation, also underlined by the presence of lateral cracks. SAED investigations exhibited a WO_3 based oxide layer for WB_{2-z} and mixed oxide scales (e.g. Ta_2O_5 as well as TaBO_4) for TaB_{2-z} films, also underlined by TEM-EDS line scans. Furthermore, TOF-ERDA measurements showed an increased amount of boron within the oxide scales for coatings with rising Ta content, suggesting for a decelerated formation of a volatile boron oxides.

In summary, the addition of Ta to WB_{2-z} based coatings retards the oxide scale kinetics through the formation of denser, less volatile, and adherent scales, thus being a key factor for the enhanced oxidation resistance. An optimum composition of $\text{W}_{1-x}\text{Ta}_x\text{B}_{2-z}$ based coatings would be in the range of $x = 0.2$ – 0.3 , combining enhanced fracture toughness ($\geq 3.0 \text{ MPa}\sqrt{\text{m}}$) as well as super hardness ($\geq 40 \text{ GPa}$) next to a decent oxidation resistance.

CRedit authorship contribution statement

C. Fuger: Conceptualization, Software, Investigation, Writing - original draft. **B. Schwartz:** Investigation. **T. Wojcik:** Investigation. **V. Moraes:** Investigation. **M. Weiss:** Investigation, Writing - review &

Appendix

See Appendix Fig. A1.

editing. **A. Limbeck:** Investigation. **C.A. Macauley:** Investigation, Writing - review & editing. **O. Hunold:** Writing - review & editing. **P. Polcik:** Writing - review & editing. **D. Primetzhofner:** Investigation, Writing - review & editing. **P. Felfer:** Investigation, Writing - review & editing. **P.H. Mayrhofer:** Writing - review & editing. **H. Riedl:** Supervision, Conceptualization, Writing - review & editing, Project administration.

Declaration of Competing Interest

The authors declare that they have no known competing financial interests or personal relationships that could have appeared to influence the work reported in this paper.

Acknowledgements

The authors greatly acknowledge the financial support of Plansee Composite Materials GmbH, Oerlikon Balzers Surface Solutions AG and the Christian Doppler Gesellschaft within the framework of the Christian Doppler Laboratory for Surface Engineering of high-performance Components. SEM and TEM investigations were carried out using facilities of the USTEM center of TU Wien, Austria. CM and PF acknowledge financial support by the Bavarian Ministry of Economic Affairs and Media, Energy and Technology for the joint projects in the framework of the Helmholtz Institute Erlangen-Nürnberg for Renewable Energy (IEK-11) of Forschungszentrum Jülich. CAM and PF would also like to acknowledge funding by the Deutsche Forschungsgemeinschaft (DFG) via the Cluster of Excellence 'Engineering of Advanced Materials' (project EXC 315). Support by VR-RFI (contracts #821-012-5144 and #2017-00646_9) and the Swedish Foundation for Strategic Research (SSF, contract RIF14-0053) supporting accelerator operation is gratefully acknowledged.

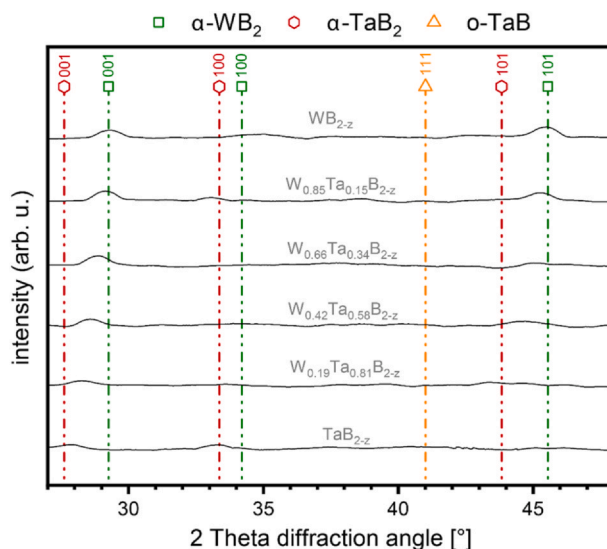


Fig. A 1. Structural evolution of $\text{W}_{1-x}\text{Ta}_x\text{B}_{2-z}$ thin films obtained by XRD analysis, realized by a Philips XPERT diffractometer in Bragg-Brentano configuration equipped with a $\text{Cu-K}\alpha$ ($\lambda = 1.54 \text{ \AA}$) radiation source. The green, red and yellow dashed vertical lines are indicating the α - WB_2 , α - TaB_2 and o - TaB phase, respectively [12].

References

- [1] I. Petrov, L. Hultman, U. Helmersson, J.-E. Sundgren, J.E. Greene, Microstructure modification of TiN by ion bombardment during reactive sputter deposition, *Thin Solid Films* 169 (1989) 299–314, [https://doi.org/10.1016/0040-6090\(89\)90713-X](https://doi.org/10.1016/0040-6090(89)90713-X).
- [2] O. Knotek, F. Löffler, H.J. Scholl, C. Barimani, The multisource arc process for depositing ternary Cr- and Ti-based coatings, *Surf. Coatings Technol.* 68–69 (1994) 309–313, [https://doi.org/10.1016/0257-8972\(94\)90178-3](https://doi.org/10.1016/0257-8972(94)90178-3).
- [3] W. Münz, Titanium aluminum nitride films: a new alternative to TiN coatings, *J. Vac. Sci. Technol. A* 4 (1986) 2717–2725, <https://doi.org/10.1116/1.573713>.
- [4] C. Mitterer, Borides in thin film technology, *J. Solid State Chem.* 133 (1997) 279–291, <https://doi.org/10.1006/JSSC.1997.7456>.
- [5] H. Euchner, P.H. Mayrhofer, Designing thin film materials-ternary borides from first principles, *Thin Solid Films* 583 (2015) 46–49, <https://doi.org/10.1016/j.tsf.2015.03.035>.
- [6] J. Nagamatsu, N. Nakagawa, T. Muranaka, Y. Zenitani, J. Akimitsu, Superconductivity at 39 K in magnesium diboride, *Nature* 410 (2001) 63–64, <https://doi.org/10.1038/35065039>.
- [7] K. Balasubramanian, S.V. Khare, D. Gall, Valence electron concentration as an indicator for mechanical properties in rocksalt structure nitrides, carbides and carbonitrides, *Acta Mater.* 152 (2018) 175–185, <https://doi.org/10.1016/j.actamat.2018.04.033>.
- [8] T. Chihai, M. Reffas, M. Fatmi, A. Bouhemadou, B. Ghebouli, M.A. Ghebouli, Brittle to ductile transition dependence upon the transition pressure of MB₂ (M=Ti, Zr, Hf, V, Nb, Ta, Cr, Mo, W) compounds, *Chin. J. Phys.* 53 (2015) 100801–100802, <https://doi.org/10.6122/CJP.20150703>.
- [9] J. Karch, R. Birringer, H. Gleiter, Ceramics ductile at low temperature (1987) 6–8.
- [10] A.L. Ivanovskii, Mechanical and electronic properties of diborides of transition 3d–5d metals from first principles: toward search of novel ultra-incompressible and superhard materials, *Prog. Mater. Sci.* 57 (2012) 184–228, <https://doi.org/10.1016/j.pmatsci.2011.05.004>.
- [11] V. Moraes, H. Riedl, C. Fuger, P. Polcik, H. Bolvardi, D. Holec, P.H. Mayrhofer, Ab initio inspired design of ternary boride thin films, *Sci. Rep.* 8 (2018) 9288, <https://doi.org/10.1038/s41598-018-27426-w>.
- [12] C. Fuger, V. Moraes, R. Hahn, H. Bolvardi, P. Polcik, H. Riedl, P.H. Mayrhofer, Influence of tantalum on phase stability and mechanical properties of WB₂, *MRS Commun.* 9 (2019) 375–380, <https://doi.org/10.1557/mrc.2019.5>.
- [13] B. Bakhit, D.L.J. Engberg, J. Lu, J. Rosen, H. Högberg, L. Hultman, I. Petrov, J.E. Greene, G. Greczynski, Strategy for simultaneously increasing both hardness and toughness in ZrB₂-rich Zr_{1-x}Ta_xW_y thin films, *J. Vac. Sci. Technol. A* 37 (2019) 031506, <https://doi.org/10.1116/1.5093170>.
- [14] T. Glechner, R. Hahn, T. Wojcik, D. Holec, S. Kolozsvári, H. Zaid, S. Kodambaka, P.H. Mayrhofer, H. Riedl, Assessment of ductile character in superhard Ta-C-N thin films, *Acta Mater.* 179 (2019) 17–25, <https://doi.org/10.1016/j.actamat.2019.08.015>.
- [15] Y.M. Liu, R.Q. Han, F. Liu, Z.L. Pei, C. Sun, Sputtering gas pressure and target power dependence on the microstructure and properties of DC-magnetron sputtered AlB₂-type WB₂ films, *J. Alloys Compd.* 703 (2017) 188–197, <https://doi.org/10.1016/j.jallcom.2017.01.337>.
- [16] Y. Liu, W. Shi, L. Tian, T. Li, C. Wang, F. Liu, Z. Pei, D. Fan, Influence of modulation period on structure and mechanical properties of WB₂/CrN films deposited by direct-current magnetron sputtering, *J. Alloys Compd.* 788 (2019) 729–738, <https://doi.org/10.1016/j.jallcom.2019.02.188>.
- [17] L.E. Pangilinan, C.L. Turner, G. Akopov, M. Anderson, R. Mohammadi, R.B. Kaner, Superhard tungsten diboride-based solid solutions, *Inorg. Chem.* 57 (2018) 15305–15313, <https://doi.org/10.1021/acs.inorgchem.8b02620>.
- [18] V. Moraes, C. Fuger, V. Paneta, D. Primetzhofer, P. Polcik, H. Bolvardi, M. Arndt, H. Riedl, P.H. Mayrhofer, Substoichiometry and tantalum dependent thermal stability of α -structured W-Ta-B thin films, *Sci. Mater.* 155 (2018) 5–10, <https://doi.org/10.1016/j.scriptamat.2018.06.005>.
- [19] L. Zauner, P. Ertelthaler, T. Wojcik, H. Bolvardi, S. Kolozsvári, P.H. Mayrhofer, H. Riedl, Reactive HiPIMS deposition of Ti-Al-N: Influence of the deposition parameters on the cubic to hexagonal phase transition, *Surf. Coatings Technol.* 382 (2020) 125007, <https://doi.org/10.1016/j.surfcoat.2019.125007>.
- [20] A. Cakara, M. Bonta, H. Riedl, P.H. Mayrhofer, A. Limbeck, Development of a multi-variate calibration approach for quantitative analysis of oxidation resistant Mo-Si-B coatings using laser ablation inductively coupled plasma mass spectrometry, *Spectrochim. Acta Part B At. Spectrosc.* 120 (2016) 57–62, <https://doi.org/10.1016/j.sab.2016.04.004>.
- [21] H. Riedl, A. Vieweg, A. Limbeck, J. Kalaš, M. Arndt, P. Polcik, H. Euchner, M. Bartosik, P.H. Mayrhofer, Thermal stability and mechanical properties of boron enhanced Mo-Si coatings, *Surf. Coatings Technol.* 280 (2015) 282–290, <https://doi.org/10.1016/j.surfcoat.2015.09.015>.
- [22] M. Bonta, J. Frank, S. Taibl, J. Fleig, A. Limbeck, Online-LASIL: laser ablation of solid samples in liquid with online-coupled ICP-OES detection for direct determination of the stoichiometry of complex metal oxide thin layers, *Anal. Chim. Acta* 1000 (2018) 93–99, <https://doi.org/10.1016/j.aca.2017.10.025>.
- [23] E. Aschauer, S. Sackl, T. Schachinger, T. Wojcik, H. Bolvardi, M. Arndt, P. Polcik, H. Riedl, P.H. Mayrhofer, Nano-structural investigation of Ti-Al-N/Mo-Si-B multilayer coatings: a comparative study by APT and HR-TEM, *Vacuum* 157 (2018) 173–179, <https://doi.org/10.1016/j.vacuum.2018.08.037>.
- [24] P. Ström, P. Petersson, M. Rubel, G. Possnert, A combined segmented anode gas ionization chamber and time-of-flight detector for heavy ion elastic recoil detection analysis, *Rev. Sci. Instrum.* 87 (2016) 103303, <https://doi.org/10.1063/1.4963709>.
- [25] M.A. Arvizu, R.-T. Wen, D. Primetzhofer, J.E. Klemberg-Sapieha, L. Martinu, G.A. Niklasson, C.G. Granqvist, Galvanostatic ion detrapping rejuvenates oxide thin films, *ACS Appl. Mater. Interfaces* 7 (2015) 26387–26390, <https://doi.org/10.1021/acsami.5b09430>.
- [26] Y. Zhang, H.J. Whitlow, T. Winzell, I.F. Bubb, T. Sajaavaara, K. Arstila, J. Keinonen, Detection efficiency of time-of-flight energy elastic recoil detection analysis systems, *Nucl. Instrum. Methods Phys. Res. Sect. B Beam Interact. Mater. Atoms* 149 (1999) 477–489, [https://doi.org/10.1016/S0168-583X\(98\)00963-X](https://doi.org/10.1016/S0168-583X(98)00963-X).
- [27] M.S. Janson, CONTES instruction manual (2004).
- [28] E. Aschauer, H. Riedl, C.M. Koller, H. Bolvardi, M. Arndt, P. Polcik, P.H. Mayrhofer, Adhesive wear formation on PVD coated tools applied in hot forming of Al-Si coated steel sheets, *Wear* 430–431 (2019) 309–316, <https://doi.org/10.1016/j.wear.2019.05.019>.
- [29] M. Thuvander, G. Östberg, M. Ahlgren, L.K.L. Falk, Atom probe tomography of a Ti-Si-Al-C-N coating grown on a cemented carbide substrate, *Ultramicroscopy* 159 (2015) 308–313, <https://doi.org/10.1016/j.ultramic.2015.04.008>.
- [30] M. Hans, J.M. Schneider, On the chemical composition of TiAlN thin films - comparison of ion beam analysis and laser-assisted atom probe tomography with varying laser pulse energy, *Thin Solid Films* 688 (2019) 137251, <https://doi.org/10.1016/j.tsf.2019.04.026>.
- [31] H. Riedl, C.M. Koller, F. Munnik, H. Hutter, F. Mendez Martin, R. Rachbauer, S. Kolozsvári, M. Bartosik, P.H. Mayrhofer, Influence of oxygen impurities on growth morphology, structure and mechanical properties of Ti-Al-N thin films, *Thin Solid Films* 603 (2016) 39–49, <https://doi.org/10.1016/j.tsf.2016.01.039>.
- [32] O. Kubaschewski, B.E. Hopkins, Oxidation mechanisms of niobium, tantalum, molybdenum and tungsten, *J. Less Common Met.* 2 (1960) 172–180, [https://doi.org/10.1016/0022-5088\(60\)90012-6](https://doi.org/10.1016/0022-5088(60)90012-6).
- [33] R. Hollerweger, H. Riedl, J. Paulitsch, M. Arndt, R. Rachbauer, P. Polcik, S. Primig, P.H. Mayrhofer, Origin of high temperature oxidation resistance of Ti-Al-Ta-N coatings, *Surf. Coatings Technol.* 257 (2014) 78–86, <https://doi.org/10.1016/j.surfcoat.2014.02.067>.
- [34] T. Tokunaga, T. Kawamoto, K. Tanaka, N. Nakamura, Y. Hayashi, K. Sasaki, K. Kuroda, T. Yamamoto, Growth and structure analysis of tungsten oxide nanorods using environmental TEM, *Nanoscale Res. Lett.* 7 (2012) 85, <https://doi.org/10.1186/1556-276X-7-85>.
- [35] M. Moldovan, C.M. Weyant, D.L. Johnson, K.T. Faber, Tantalum oxide coatings as candidate environmental barriers, *J. Therm. Spray Technol.* 13 (2004) 51–56, <https://doi.org/10.1007/s11666-004-0049-z>.